Fluorescent molecular rotors

From working principles to visualization of mechanical contacts

Suhina, T.

Publication date
2017

Document Version
Other version

License
Other

8

Fluorescent Molecular Rotors reveal Deviations from Amontons' Law*

Abstract

In this chapter, we demonstrate how fluorescent molecular probes are used to solve one of the most challenging problems in contact mechanics, namely deviations from Amonton's law and the relation between friction and real contact area. The goal of this chapter is not to provide a rigorous description of conducted experiments and the existing literature on this topic (as the simulations and many of the experiments were not conducted by the author of this thesis), but to serve as a closing chapter which demonstrates the applicability of the system that we developed (Chapters 3 and 7) towards understanding friction mechanics.

* This chapter is adapted from:
Weber, B.; Suhina, T.; Junge, T.; Pastewka, L.; Brouwer, A. M. and Bonn, D. *Submitted*

8.1 Introduction

Approximately one third of the world's energy consumption is lost to friction, but our fundamental understanding of how this friction emerges is not complete.[1] Friction is commonly described in terms of Amontons' law, which defines a material-dependent constant, the friction coefficient μ, as the ratio between friction force and normal force.[2] Amontons' law is commonly explained with the two non-trivial assumptions that both the frictional and normal force depend linearly on the real contact area between the two sliding surfaces.[3,4] Most surfaces are rough[3,5–10] and experimental testing of frictional contact models has proven difficult, because few in-situ experiments are able to resolve this real contact area. All frictional theories ultimately aim to understand how frictional dissipation emerges from the details of contacts between two sliding surfaces. Experimental testing of such contact theories for rough interfaces is crucial, but has proven very challenging. In the late 19th and early 20th century electrical conductivity has been used as a measure of the contact area between metal surfaces.[11] More recently, optical techniques such as phase-contrast microscopy,[12] frustrated total internal reflection[13] or interferometry[14] have been used to gain insight into contact and friction mechanics. However, two important aspects of contact mechanics and their relation to friction were difficult to address by these experiments due to limited spatial resolution. First, can deformations of the roughness be elastically transferred from one contact point to another and thereby influence the contact area? Second, what is the relative importance of plasticity and elasticity in the formation of contact area and friction?

Answering these questions requires a detailed experimental observation of the real contact area. The contact imaging method that we developed (see Chapters 3 and 7) enables us to independently probe the two relations that form the microscopic origin of Amontons' law. While the friction force is proportional to the real contact area, we find that this real contact area does not increase linearly with normal force. Contact simulations show that the breaking of Amontons' law is due to both elastic interactions between asperities on the surface and contact plasticity of the asperities. Contact area and fine details of the measured contact geometry are exactly reproduced by including plastic hardening into the simulations. These new insights into contact mechanics pave the way for a quantitative microscopic understanding of contact mechanics and tribology.

8.2 Results and discussion

In the experiments, we chemically attach molecules shown in Scheme 8.1 to the surface of very smooth and flat glass cover slips,[15] which are then inserted into our microscopy setup (illustrated in Chapter 1, Fig. 1.5 and Chapter 7, Fig. 7.1). A sphere is lowered into contact with the cover slip wetted with a polar liquid (to reduce light scattering at the surface) and the contact is illuminated from below, to excite the monolayer of rigidochromic molecules at the surface of the

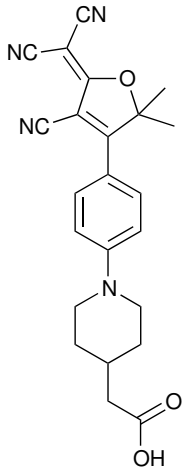

Scheme 8.1: Molecular rotor used in this work.

cover slip. The molecules confined by the sphere fluoresce very strongly within the contact zone, whereas practically no fluorescence can be observed outside of the contact. Compared to frustrated total internal reflection used for contact detection in other experiments,[16] rigidochromic molecules are more than an order of magnitude more accurate in detecting contacts in the axial (z-) direction. This is easily demonstrated by monitoring the excitation light that gets reflected by the interface between the sphere and the contact immersion liquid or the substrate and the contact immersion liquid. The interference between these two contributions leads to a ring shaped intensity pattern around the contact, commonly known as Newton rings. Such a pattern in shown in Fig. 8.1. These rings have maximal intensity where the gap between the sphere and the substrate is equal to:[17]

$$d = (m + \frac{1}{2})\frac{\lambda}{2n}, \tag{8.1}$$

where $m = 0, 1, 2, ...$ is the ring number, $\lambda = 488$ nm is the wavelength of reflected light and $n = 1.447$ is refractive index of the immersion liquid (in our case formamide). We consider a line profile that runs through the center of the contact and extract the points at which the line intersects with the Newton rings. Such intensity profile is shown in Fig. 8.2 a) (blue line) and compared with the fluorescence response (green line) of our confined molecules. We use the Otsu thresholding to separate fluorescence intensity from the background (shown as dashed lines in Fig. 8.2 a)). Using Eq. 8.1, these intersection points then give us the profile of the gap between the sphere and the substrate, close to the contact. By interpolating this profile towards the edge of the contact (Fig. 8.2 b)), as defined by the thresholded fluorescence signal (green squares in Fig. 8.2 a) and b)), we obtain the gap at which the rigidochromic molecules light up. The average gap estimated from 20 different profiles was 9 nm at the location where the fluorescence intensity indicates

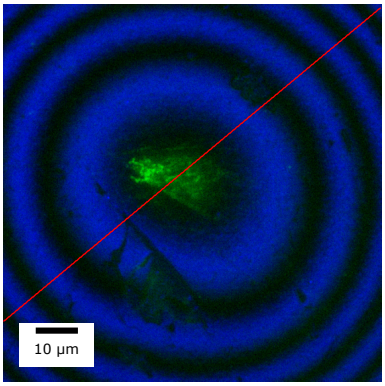

Figure 8.1: Fluorescence (green) and reflections (blue) measured at the contact between a 4 mm glass sphere and a rigidochromic cover slip (image size $90\times90\mu$m).

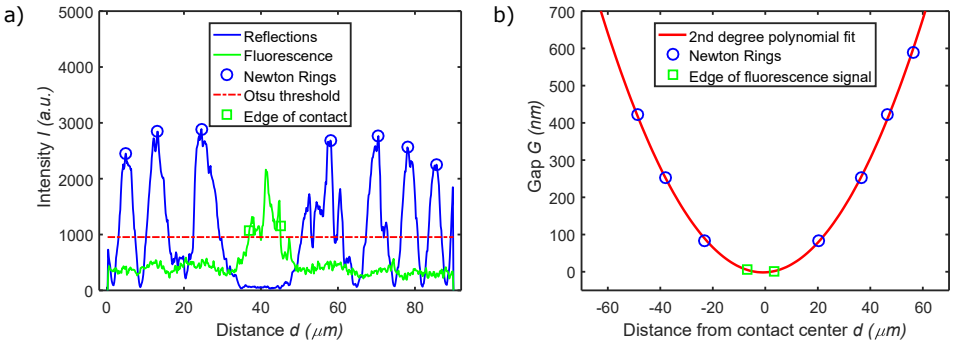

Figure 8.2: Intensity profile and gap extrapolation. a) The fluorescence (green) and the reflections (blue) along the line profile. Blue circles indicate the positions of maximum intensity for each Newton ring. b) Gap calculated from Eq. 8.1 vs. the distance from the contact centre.

the edge of the contact. This number is of the same order of magnitude as the combined roughness of the sphere and the float glass cover slip used in this experiment. From this, we conclude that the molecules fluoresce when the gap between sphere and cover slip becomes of the order of the molecule size. The integrated fluorescence intensity therefore is a direct measure of the molecular contact area. For comparison, the smallest Newton ring (reflection, Fig. 8.2 a) and b)) indicates a gap of 84 nm between the sphere and the cover slip. In the x-y plane, we resolve the contact structure with diffraction limited microscopy (based on point-spread function, we estimate our lateral resolution to be ∼450 nm). The fact that contact pixel intensities do not vary spatially or with load, indicates that there is not much contact structure below this scale.

In the experimental range of normal forces, the real contact area evolves from a discrete collection of asperities in contact at 4 mN to an almost Hertzian[18]

contact circle at 400 mN. This is quantitatively demonstrated in Fig. 8.3, where we press a PMMA bead (radius = 0.75 mm) onto the functionalized cover slip. During this evolution, existing contacts deform and increase their area while new contact patches emerge elsewhere. Quite surprisingly and contrary to the common interpretation of Amontons' law, the real contact area does not increase linearly with the normal force. This is shown in Fig. 8.4 a). Squares, triangles and circles represent experiments on three similar polystyrene spheres, while solid lines show values obtained from different theories (see below). The inset shows the same data on a logarithmic scale. Experimental contact is reproduced by the contact hardening model that considers long range elastic asperity interactions and local plasticity at contact (see below). Other models either underestimate the contact area or do not describe the deviation from linearity found in the experiment.

If the contact area links the normal force to the friction force, this observation would imply that Amontons' law is broken. To induce frictional slip and measure the friction coefficient, we rotate the rheometer plate at a constant velocity of 1 μm/s (see Chapter 1, Fig. 1.5) resulting in a linear build up of friction force, caused by the finite stiffness of the measurement system (inset Fig. 8.4 b)). Once the applied force exceeds the static friction, the contacts break and slip. We indeed observe that Amontons' law is broken; the static friction force is proportional to the contact area but not to the normal force (Fig. 8.4 b)). This means that the friction coefficient is ill-defined, as it depends on the normal force.

The experiments thus show that friction is controlled by the contact area, but not what sets the contact area. Many of our present-day insights into the mechanics of rough contacts come from theoretical considerations. Early models assumed that surfaces deform purely plastically.[3,5] These models assume that surface roughness causes the contact area to be small, which results in large pressures within the contact zone, which leads to irreversible (plastic) deformation of the contact points. The real contact area A is then proportional to the load N pushing the surfaces together, ($A = N/p_\gamma$). In this expression p_γ is the penetration hardness of the material. It was initially argued that after the first, irreversible deformation of the material, the material deforms elastically. This assumption led to the development of sophisticated multi-asperity models.[6–8,19,20] These theories describe surface roughness as a collection of identical, non-interacting, spherical summits of random height that follow elastic, Hertzian[18] contact mechanics. Persson's recent scaling theory[21] alternatively, uses a description with an arbitrary form for the roughness, taking into account elastic interactions between asperities on different length scales. Both multi-asperity and Persson theory also predict proportionality $A = N/p_{\mathrm{rough}}$ with the characteristic pressure $p_{rough} = E^*/2\ h'_{\mathrm{rms}}$. According to this theory, the real contact area is governed by normal load N, elastic contact modulus E^*, and root mean square slope of the surface roughness h'_{rms}.

To investigate why in the experiments proportionality between contact area and normal force is not observed, simulations in which different effects can be considered or left out were performed by our coworkers Junge and Pastewka. Prior to the contact experiment, we use atomic force microscopy (AFM) to obtain a three dimensional map of the sphere roughness at the exact same location that is pressed

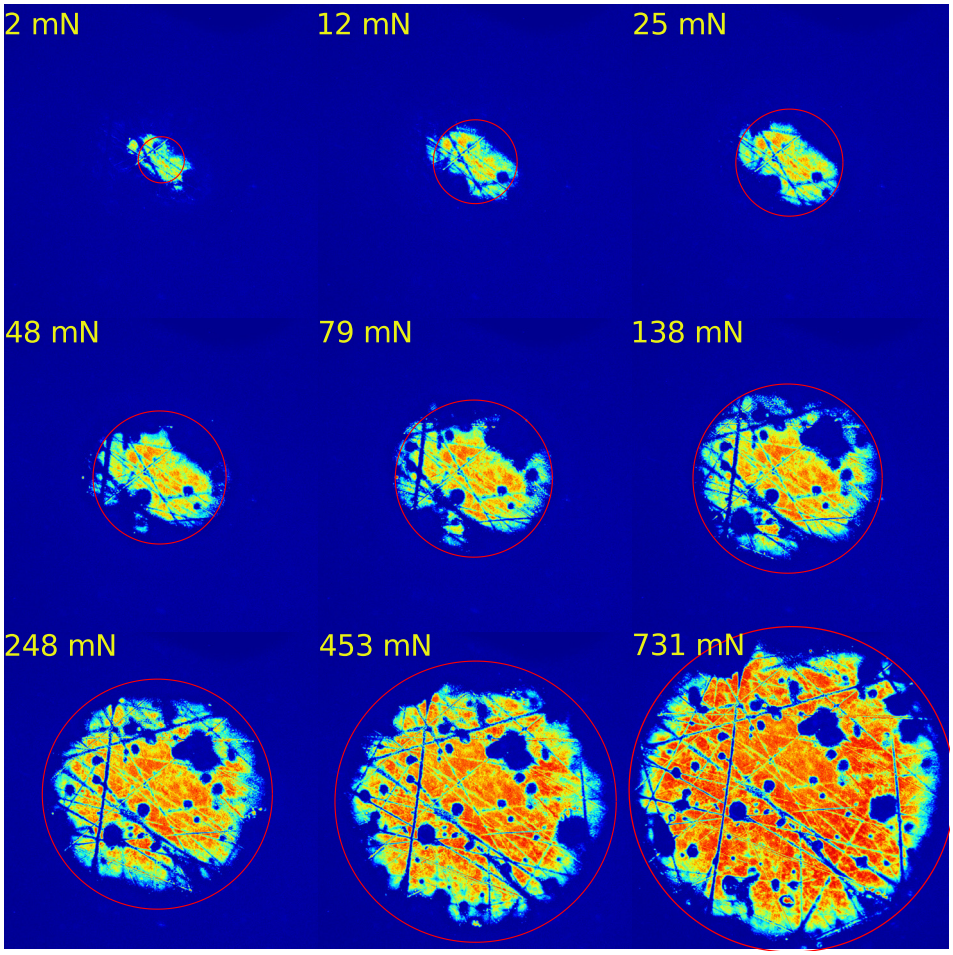

Figure 8.3: Measurement of the real contact area obtained by pressing a PMMA bead onto a functionalized cover slip.

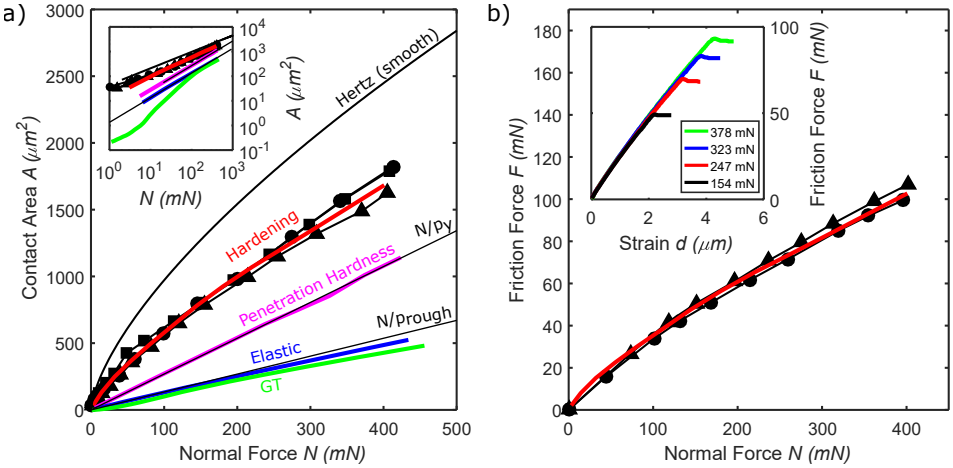

Figure 8.4: Amontons' law and the real contact area. a) Real contact area *vs* normal force; b) static friction force of contacts like those in (a), measured at different normal forces. See text for details.

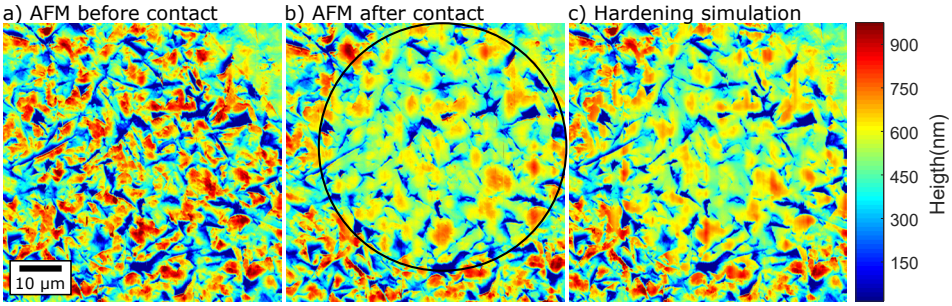

Figure 8.5: AFM image of the polystyrene bead mesured a) before contact formation; b) after contact formation; c) predicted by strain-hardening simulation.

onto the glass (see Fig. 8.5 a)). Since we use materials for the sphere that are significantly softer and rougher than the glass, the deformation of this roughness map completely determines the experimental contact area and therefore forms the ideal input for contact simulations. We first consider elasticity and start with the rough-sphere multi-asperity model of Greenwood & Tripp[19] to compute the dependence of the contact area on normal force. Surprisingly, the contact area resulting from this calculation (Fig. 8.6 b)) is five times smaller than that found in the experiment (Fig. 8.6 a)). By reducing rough surfaces to a collection of discrete asperities, multi-asperity theories such as the Greenwood & Tripp model ignore strain transmitted from asperity to asperity through the bulk.

The omission of such interactions from multi-asperity theories is considered to be problematic,[21] because many surfaces are fractal; smaller asperities exist on top of larger asperities implying that in contact, asperities have to transmit

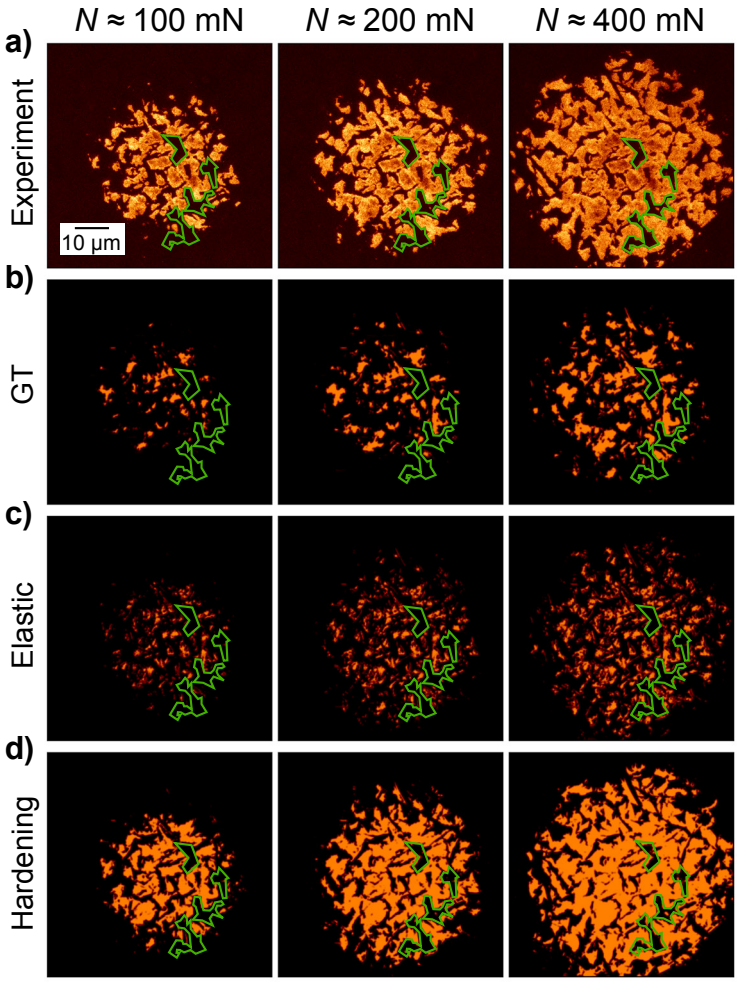

Figure 8.6: Measured and simulated real contact area at different normal loads. a) Fluorescence intensity images of the contact; b) elastic Greenwood-Tripp simulation of the contact area; c) Elastic simulation with interacting asperities; d) strain-hardening simulation.

strain to one another. We therefore compare the Greenwood & Tripp model to a full numerical calculation of the contact area using a Green's function method[22] that treats the elastic interaction exactly on all length scales. This simulation ignores nonlinear elastic effects but constitutes the exact mathematical solution of the problem that both multi-asperity theories and Persson's analysis approximate. There are no adjustable parameters in the elastic simulation, because sphere radius, sphere roughness and modulus are all independently measured. We observe that the inclusion of asperity interactions leads to a different contact patch distribution (Fig. 8.6 c)) compared to that of the Greenwood & Tripp model. The contact morphology obtained by elastic simulation is closer to the experiment, leading us to conclude that asperity interactions are required to more accurately predict the real contact area. The real contact area from the elastic simulations, however, is still linear in normal force and still significantly smaller than in the experiment (Fig. 8.6 a)).

Due to large stresses at the contact points ($\sim$ 200 MPa), plastic deformation of the polystyrene bead may occur (penetration hardness of polystyrene is of the same order of magnitude[23]) in addition to elastic deformation. To confirm that plasticity is indeed important in the experiment, we measured the surface topography by AFM after the contact experiment, which shows permanent deformation of the contact points (Fig. 8.5 b)). For this reason, we tested purely plastic contact deformation effect in our simulations. We varied penetration hardness (p_γ) as the only adjustable parameter, but could not achieve agreement with our experimental results.

From the purely plastic deformation model, one would expect that the contact pressure remains constant at the value of the penetration hardness of the material. In our experiment, however, the dependence of real contact area on load is sub-linear. For this reason, the average contact pressure changes during our experiments, which suggests that the contacts become harder to deform at large strains. This effect is generally observed for polystyrene.[24] To describe this effect, we define linear hardening with local plastic displacement $p_\gamma = kh$ and adjust k to match our experimental contact area *vs* load curves. Such simulations are able to reproduce measured contact area (Figs. 8.5 and 8.6 a) and d)) and deviations from linearity of contact area with load (Fig. 8.4 a)). This way, we are able to predict where the contact will occur using only surface topography as input. The strain-hardening model also describes the contact mechanics of poly(methyl methacrylate), and we have observed sub-linear dependence of real contact area on load for polytetrafluoroethylene and glass, which indicates that these materials behave similarly to polystyrene (see ref. 25 for description of these experiments).

8.3 Conclusion

To summarize, molecular rotors covalently attached to the glass surface enable us to image frictional contact with molecular resolution in the axial (z-) direction, and diffraction-limited lateral (x-y) resolution. Our results show that static friction is

directly proportional to the real contact area. The contact area, however, does not grow linearly with normal load. Simulations show that this stems from elasto-plastic nature of deformations that constitute the surface roughness. Real contact area can only be accurately predicted when both elastic deformations between the asperities (ignored in multi-asperity models) and strain-hardening of the material (ignored in most numerical calculations) are taken into account. While the elastic behavior is expected to be observed in most other materials, surface plasticity may be material-dependent.

References

1. Szeri, A. Z. *Tribology: friction, lubrication, and wear*; McGraw-Hill, 1980.
2. Amontons, G. *De la resistance causée dans les machines*; Mem. l'Académie R. A, 1699.
3. Bowden, F.; Tabor, D. *Proc. R. Soc. A* **1939**, 391–413.
4. Gao, J.; Luedtke, W.; Gourdon, D.; Ruths, M.; Israelachvili, J.; Landman, U. *J. Phys. Chem. B* **2004**, *108*, 3410–3425.
5. Holm, R. *Electric contacts: theory and application*; Springer Science & Business Media, 1967.
6. Greenwood, J.; Williamson, J. *Proc. R. Soc. A* **1966**, 300–319.
7. Whitehouse, D. J.; Archard, J. *Proc. R. Soc. A* **1970**, *316*, 97–121.
8. Bush, A.; Gibson, R.; Thomas, T. *Wear* **1975**, *35*, 87–111.
9. Hyun, S.; Robbins, M. O. *Tribol. Int.* **2007**, *40*, 1413–1422.
10. Persson, B.; Albohr, O.; Tartaglino, U.; Volokitin, A.; Tosatti, E. *Journal of Physics: Condensed Matter* **2004**, *17*, R1.
11. Bidwell, S. *Proceedings of the Royal Society of London* **1883**, *35*, 1–18.
12. Dyson, J.; Hirst, W. *Proceedings of the Physical Society. Section B* **1954**, *67*, 309.
13. Rubinstein, S. M.; Cohen, G.; Fineberg, J. *Nature* **2004**, *430*, 1005–1009.
14. Ovcharenko, A.; Halperin, G.; Etsion, I.; Varenberg, M. *Tribology Letters* **2006**, *23*, 55–63.
15. Suhina, T.; Weber, B.; Carpentier, C. E.; Lorincz, K.; Schall, P.; Bonn, D.; Brouwer, A. M. *Angew. Chem. Int. Ed.* **2015**, *54*, 3688–3691.
16. Rubinstein, S. M.; Shay, M.; Cohen, G.; Fineberg, J. *Int. J. Fract.* **2006**, *140*, 201–212.
17. Jenkins, F.; White, H. *Fundamentals of Optics*; International student edition; McGraw-Hill, 1976.
18. Hertz, H. *J. Reine Angew. Math.* **1881**, *92*, 156–171.
19. Greenwood, J. A.; Tripp, J. H. *J. Appl. Mech.* **1967**, *34*, 153–159.
20. Greenwood, J.; Tripp, J. *Proc. Inst. Mech. Eng.* **1970**, *185*, 625–633.
21. Persson, B. N. *J. Chem. Phys.* **2001**, *115*, 3840–3861.

22. Pastewka, L.; Robbins, M. O. *Appl. Phys. Lett.* **2016**, *108*, 221601.
23. McClintock, F.; Argon, A. *Mechanical behavior of materials*; Addison-Wesley Pub. Co., 1966.
24. van Melick, H.; Govaert, L.; Meijer, H. *Polymer* **2003**, *44*, 2493 – 2502.
25. Weber, B.; Suhina, T.; Junge, T.; Pastewka, L.; Brouwer, A. M.; Bonn, D. *Submitted* **2017**,